

Upper limit on axion-photon coupling from Markarian 421

Hai-Jun Li,^{1,*} Wei Chao,^{2,†} and Yu-Feng Zhou^{1,3,4,5,‡}¹Key Laboratory of Theoretical Physics, Institute of Theoretical Physics,
Chinese Academy of Sciences, Beijing 100190, China²Center for Advanced Quantum Studies, Department of Physics,
Beijing Normal University, Beijing 100875, China³School of Physical Sciences, University of Chinese Academy of Sciences, Beijing 100049, China⁴School of Fundamental Physics and Mathematical Sciences,

Hangzhou Institute for Advanced Study, UCAS, Hangzhou 310024, China

⁵International Centre for Theoretical Physics Asia-Pacific, Beijing/Hangzhou, China

(Dated: June 4, 2024)

The pseudo-Nambu-Goldstone boson (pNGB), axions, are motivated candidates for physics beyond the Standard Model (SM). The QCD axion [1, 2] was originally postulated to solve the strong CP problem, meanwhile, it is the cold dark matter (DM) candidate. Additionally, the axionlike particle (ALP) can also account for the DM, but is not associated to the solution of the strong CP problem. For simplicity, in the following the “axion” stands for the ALP. The axion-photon interaction has a two-photon vertex

$$\mathcal{L} \supset -\frac{1}{4}g_{a\gamma}aF_{\mu\nu}\tilde{F}^{\mu\nu}, \quad (1)$$

where a is the axion field, $g_{a\gamma}$ is the axion-photon coupling constant, $F_{\mu\nu}$ is the electromagnetic field tensor and its dual tensor $\tilde{F}^{\mu\nu} = \frac{1}{2}\epsilon^{\mu\nu\rho\sigma}F_{\rho\sigma}$. Considering the interaction between the axion and very high energy (VHE) photon in the astrophysical magnetic fields, it can lead to some detectable effects, such as the reduced TeV opacity of the Universe [3–5]. The VHE TeV gamma-ray emissions from the extragalactic space, such as the active galactic nuclei (AGN), are mainly affected by the effect of extragalactic background light (EBL) absorption through the electron-positron pair production process $\gamma_{\text{TeV}} + \gamma_{\text{EBL}} \rightarrow e^+ + e^-$. If considering the axion-photon conversion and further back-conversion in several astrophysical magnetic fields, the EBL absorption effect can be reduced and the Universe would appear to be more transparent than expected based on the pure EBL absorption. Meanwhile, it also provides a natural mechanism to constrain the axion properties with the axion mass m_a and the coupling $g_{a\gamma}$. See Fig. 1 for the latest axion-photon limits in the $\{m_a, g_{a\gamma}\}$ plane.

In this letter, we obtain a stringent upper limit on axion-photon coupling from the TeV blazar Markarian 421 with the 1038 days VHE gamma-ray observations. The source Markarian 421 (R.A. = 11^h04^m27.31^s, Dec. = +38°12′31.8″, J2000) is a well-known nearby blazar at a redshift $z = 0.031$, it also known as other names, Mrk 421, TeV J1104+382, and 1ES 1101+384. Markarian 421 belongs to a subclass of AGNs, the high-frequency peaked BL Lac (HBL) or the high-synchrotron peaked BL Lac (HSP) object, which are classified by the

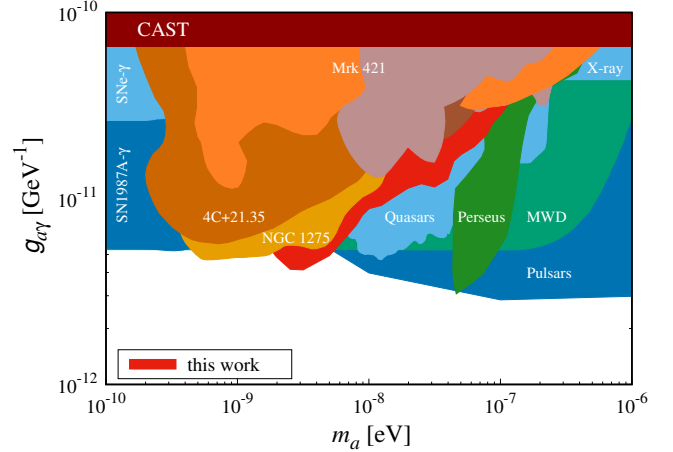


FIG. 1. The axion-photon limits in the $\{m_a, g_{a\gamma}\}$ plane. The red contour represents the 99% C.L. limit set by Markarian 421 with the 1038 days VHE gamma-ray observations measured by Fermi-LAT and HAWC. Other limits in the plane are taken from Ref. [6].

weak or missing broad emission lines in the optical spectra. It was first discovered with the VHE emission by the Whipple 10-m Observatory [7]. Many works were investigated to constrain the axion-photon coupling from the gamma-ray of Markarian 421 [8, 9]. Recently, its long-term gamma-ray spectra are measured by the collaborations, the Large Area Telescope on board NASA’s Fermi Gamma-ray Space Telescope (Fermi-LAT) and the High Altitude Water Cherenkov (HAWC) Gamma-Ray Observatory, with the 1038 days of exposure from 2015 June to 2018 July [10]. Using this long-term gamma-ray flux, we consider the axion-photon conversion effect on the spectral energy distributions (SEDs) and set the limit on axion-photon coupling.

We first show the long-term VHE gamma-ray observations of Markarian 421 under the null hypothesis. The experimental data of Markarian 421 measured by Fermi-LAT and HAWC are shown in Fig. 2. To fit the gamma-ray spectrum, the intrinsic spectral model is selected as the power law with a super-exponential cut-off (SEPWL), $\Phi_{\text{int}}(E) = N_0(E/E_0)^{-\Gamma} \exp(-(E/E_c)^d)$,

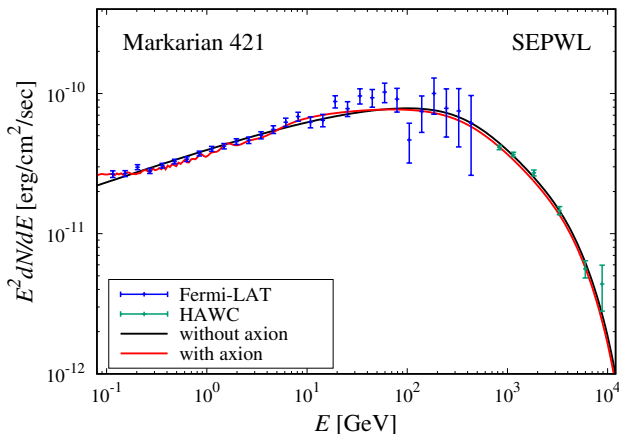


FIG. 2. The best-fit VHE gamma-ray SEDs of Markarian 421 under the null and axion hypotheses. The black and red lines represent the best-fit SEDs without/with the axion-photon conversion, respectively. The blue and green experimental data are taken from Fermi-LAT and HAWC [10], respectively.

where E represents the VHE photon energy, N_0 is a normalized constant, Γ is the spectral index, E_0 , E_c , and d are free parameters, and we fix $E_0 = 1$ GeV. As mentioned before, the main effect on VHE photon in the extragalactic space is the EBL photon absorption effect with an absorption factor $e^{-\tau}$, where τ is the optical depth, and the EBL spectral model is taken as Franceschini-08 [11]. Then we have the chi-square value under the null hypothesis $\chi_{\text{null}}^2 = \sum_{i=1}^N ((e^{-\tau} \Phi_{\text{int}}(E_i) - \psi(E_i))/\delta(E_i))^2$, where $N = 36$ (Fermi-LAT: 30, and HAWC: 6) represents the gamma-ray spectral point number, ψ and δ represent the detected flux and its uncertainty, respectively. Note that here the gamma-ray intrinsic spectral model $\Phi_{\text{int}}(E)$ is selected with the minimum best-fit reduced χ_{null}^2 from several common spectral models, see the Supplemental Material. We show the best-fit gamma-ray SED of Markarian 421 in Fig. 2. The black line represents the best-fit SED under the null hypothesis with $\chi_{\text{null}}^2 = 44.24$ and $\chi_{\text{null}}^2/\text{d.o.f.} = 1.38$, where d.o.f. is the degree of freedom.

Next, we consider the effects of axion-photon conversion on VHE gamma-ray propagations from the source Markarian 421 to the Earth. In the transverse homogeneous magnetic field, the axion-photon conversion probability can be simply characterized as $\mathcal{P}_{a\gamma} = (g_{a\gamma} B_T L_{\text{osc}}/2\pi)^2 \sin^2(\pi x_3/L_{\text{osc}})$, where B_T is the transverse magnetic field, L_{osc} is the oscillation length, and x_3 is the direction of the axion-photon propagation. While in the non-homogeneous astrophysical magnetic field, the magnetic field can be modeled as the domain-like structure and each domain can be regarded as homogeneous. In this case, the final photon-axion-photon conversion probability (the final photon survival probability) can be described in the density matrix formal

$\mathcal{P}_{\gamma\gamma} = \text{Tr}((\rho_{11} + \rho_{22})\mathcal{T}(s)\rho(0)\mathcal{T}^\dagger(s))$, where s represents the propagation distance, $\mathcal{T}(s) = \prod_i \mathcal{T}_i(s_i)$ represents the whole transfer matrix, $\rho(0) = \text{diag}(1, 1, 0)/2$ and $\rho(s) = \mathcal{T}(s)\rho(0)\mathcal{T}^\dagger(s)$ represent the initial and final axion-photon density matrices, respectively, and $\rho_{ii} = \text{diag}(\delta_{i1}, \delta_{i2}, 0)$. In this work, the axion-photon propagation process from Markarian 421 to the Earth can be divided into three parts, the blazar jet magnetic field, the extragalactic space, and the magnetic field in the Milky Way. We first discuss the axion-photon conversion in the blazar jet magnetic field of Markarian 421, which can be described by the poloidal and toroidal components. Here we consider a transverse magnetic field model $B(r) = B_0(r/r_{\text{VHE}})^{-1}$ with an electron density model $n_{\text{el}}(r) = n_0(r/r_{\text{VHE}})^{-2}$, where $r_{\text{VHE}} \simeq R_{\text{VHE}}/\theta_{\text{jet}}$ corresponds to the distance from the source central black hole to the VHE emission region, R_{VHE} represents the radius of the VHE emission region, θ_{jet} represents the angle between the jet axis and the line of sight, B_0 and n_0 correspond to the core magnetic field and electron density at r_{VHE} , respectively. We also consider the energy transformation between the laboratory and co-moving frames, E_L and E_j , with the Doppler factor $\delta_D = E_L/E_j$. For Markarian 421, we take $B_0 = 24 \pm 6$ mG, $n_0 \simeq 1 \times 10^3 \text{ cm}^{-3}$, $R_{\text{VHE}} = 0.5 \times 10^{17} \text{ cm}$, $\theta_{\text{jet}} = 2.0^\circ$, $r_{\text{VHE}} \simeq 14.3 \times 10^{17} \text{ cm}$, and $\delta_D = 25 \pm 1$ [10]. Note that for the jet region at $r > 1$ kpc, the magnetic field is weak and can be taken as zero. Then for the host galaxy region of Markarian 421, we neglect the axion-photon conversion in this part. Secondly, in the extragalactic space, we just consider the EBL absorption effect on VHE photon through the pair-production process. Since the magnetic field strength in this region is small $\sim \mathcal{O}(1)$ nG, the axion-photon conversion effect will be weak and can be neglected. Thirdly, in the magnetic field of the Milky Way, we consider the axion-photon conversion again. Here the Galactic magnetic field is simulated with the disk and halo components, and also the ‘‘X-field’’ component at the Galactic center [12, 13].

Using the final photon survival probability $\mathcal{P}_{\gamma\gamma}$ discussed above, now we can obtain the chi-square value under the axion hypothesis $\chi_{\text{axion}}^2 = \sum_{i=1}^N ((\mathcal{P}_{\gamma\gamma} \Phi_{\text{int}}(E_i) - \psi(E_i))/\delta(E_i))^2$. For one axion $\{m_a, g_{a\gamma}\}$ parameter set, we can derive the best-fit chi-square χ_{axion}^2 , and also the best-fit chi-square distribution in the parameter plane. In Fig. 3, we show the best-fit chi-square distribution for Markarian 421 in the $\{m_a, g_{a\gamma}\}$ plane, where the label ‘‘*’’ represents the minimum best-fit chi-square $\chi_{\text{min}}^2 = 31.47$ at $\{m_a \simeq 2.5 \times 10^{-9} \text{ eV}, g_{a\gamma} \simeq 2.5 \times 10^{-11} \text{ GeV}^{-1}\}$. Meanwhile, we also show the best-fit gamma-ray SED corresponding to χ_{min}^2 in Fig. 2 with the red line. Compared with the null hypothesis $\chi_{\text{null}}^2 = 44.24$ (black line), the minimum best-fit chi-square under the axion hypothesis can be significantly depressed. Using the best-fit chi-square distribution, here we set the 99% confidence level (C.L.) limit on axion-photon coupling. In order to ob-

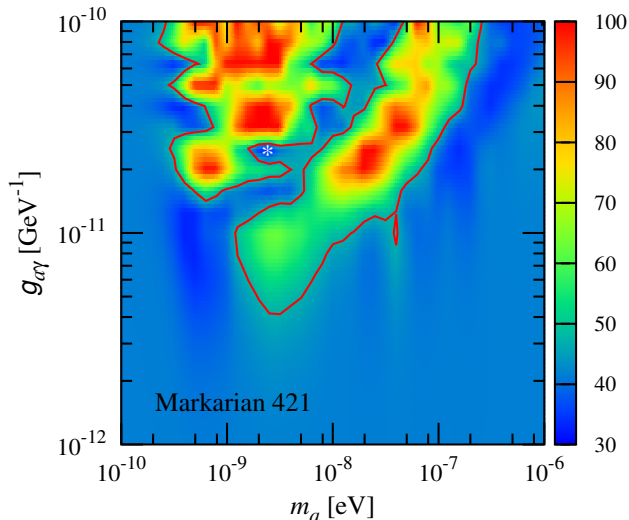


FIG. 3. The best-fit chi-square χ_{axion}^2 distribution in the $\{m_a, g_{a\gamma}\}$ plane for Markarian 421. The red contours represent the 99% C.L. exclusion regions. The label “*” corresponds to the minimum best-fit chi-square $\chi_{\text{min}}^2 = 31.47$ at $\{m_a \simeq 2.5 \times 10^{-9} \text{ eV}, g_{a\gamma} \simeq 2.5 \times 10^{-11} \text{ GeV}^{-1}\}$.

tain the value of the threshold chi-square $\chi_{99\%}^2$, 400 sets of the VHE gamma-ray observations of Markarian 421 in the pseudo-experiments by Gaussian samplings are simulated to derive the distribution of the test statistic (TS), $\text{TS} = \hat{\chi}_{\text{null}}^2 - \hat{\chi}_{\text{axion}}^2$, where $\hat{\chi}_{\text{null}}^2$ and $\hat{\chi}_{\text{axion}}^2$ are the best-fit chi-squares of the null and axion hypotheses in the Monte Carlo simulations, respectively. It obeys the non-central chi-square distribution with the non-centrality λ and the effective d.o.f., and we use it to derive the 99% C.L. chi-square difference $\Delta\chi_{99\%}^2$. Then the 99% C.L. threshold chi-square is given by $\chi_{99\%}^2 = \chi_{\text{min}}^2 + \Delta\chi_{99\%}^2$. In our simulations, we have the non-centrality $\lambda = 0.01$ and the effective d.o.f. = 5.29, indicating the threshold chi-square $\chi_{99\%}^2 = 46.98$ (see the Supplemental Material). Then we show in Fig. 3 the 99% C.L. limit with the red contours, the region in the contour is excluded. Finally, we have the 99% C.L. upper limit on axion-photon coupling set by Markarian 421 with the 1038 days VHE gamma-ray observations measured by Fermi-LAT and HAWC, which is constrained to the coupling constant

$$g_{a\gamma} \lesssim 4.0 \times 10^{-12} \text{ GeV}^{-1} \text{ (99\% C.L.)}, \quad (2)$$

for the axion mass

$$[1.0 \times 10^{-9} \text{ eV} \lesssim m_a \lesssim 1.0 \times 10^{-8} \text{ eV}]. \quad (3)$$

Compared with the latest axion-photon limits in the $\{m_a, g_{a\gamma}\}$ plane, see also Fig. 1 with the red contour, it is the most stringent upper limit in this mass region. In addition, we also have an upper limit $g_{a\gamma} \lesssim 1.5 \times 10^{-11} \text{ GeV}^{-1}$ for the axion mass $[2.0 \times 10^{-10} \text{ eV} \lesssim m_a \lesssim 1.0 \times 10^{-8} \text{ eV}]$.

In summary, we have obtained a stringent upper limit on axion-photon coupling from the 1038 days gamma-ray observations of the TeV blazar Markarian 421. The long-term VHE gamma-ray spectra are measured by the collaborations Fermi-LAT and HAWC from 2015 June to 2018 July. We show the best-fit SEDs of Markarian 421 under the null and axion hypotheses. Then we set the axion-photon limit in the $\{m_a, g_{a\gamma}\}$ plane. The 99% C.L. upper limit set by Markarian 421 is $g_{a\gamma} \lesssim 4.0 \times 10^{-12} \text{ GeV}^{-1}$ for the axion mass $[1.0 \times 10^{-9} \text{ eV} \lesssim m_a \lesssim 1.0 \times 10^{-8} \text{ eV}]$. It is the most stringent upper limit in this axion mass region. Additionally, since the VHE gamma-ray observations of another TeV blazar Markarian 501 (with redshift $z = 0.034$) at the same time are given in Ref. [10], we also make the axion analysis for this source in the Supplemental Material but no stringent limits are obtained. See also the Supplemental Material for more details in the calculations.

Acknowledgments.—We thank Sara Coutiño de León for providing the experimental data of Fermi-LAT and HAWC. This work was supported by the National Key R&D Program of China (Grant No. 2017YFA0402204), the CAS Project for Young Scientists in Basic Research YSBR-006, and the National Natural Science Foundation of China (NSFC) (Grants No. 11775025, No. 11821505, No. 11825506, No. 12047503, and No. 12175027).

* lihaijun@itp.ac.cn

† chaowei@bnu.edu.cn

‡ yfzhou@itp.ac.cn

- [1] R. Peccei and H. R. Quinn, *Phys. Rev. D* **16**, 1791 (1977).
- [2] R. Peccei and H. R. Quinn, *Phys. Rev. Lett.* **38**, 1440 (1977).
- [3] A. Mirizzi, G. G. Raffelt, and P. D. Serpico, *Phys. Rev. D* **76**, 023001 (2007), arXiv:0704.3044 [astro-ph].
- [4] D. Hooper and P. D. Serpico, *Phys. Rev. Lett.* **99**, 231102 (2007), arXiv:0706.3203 [hep-ph].
- [5] M. Ajello et al. (Fermi-LAT), *Phys. Rev. Lett.* **116**, 161101 (2016), arXiv:1603.06978 [astro-ph.HE].
- [6] C. O’HARE, “cajohare/axionlimits: Axionlimits,” (2020).
- [7] M. Punch et al., *Nature* **358**, 477 (1992).
- [8] H.-J. Li, J.-G. Guo, X.-J. Bi, S.-J. Lin, and P.-F. Yin, *Phys. Rev. D* **103**, 083003 (2021), arXiv:2008.09464 [astro-ph.HE].
- [9] L.-Q. Gao, X.-J. Bi, J.-G. Guo, W. Lin, and P.-F. Yin, *Phys. Rev. D* **109**, 063003 (2024), arXiv:2309.02166 [astro-ph.HE].
- [10] A. Albert et al. (HAWC), *Astrophys. J.* **929**, 125 (2022), arXiv:2106.03946 [astro-ph.HE].
- [11] A. Franceschini, G. Rodighiero, and M. Vaccari, *Astron. Astrophys.* **487**, 837 (2008), arXiv:0805.1841 [astro-ph].
- [12] R. Jansson and G. R. Farrar, *Astrophys. J.* **757**, 14 (2012), arXiv:1204.3662 [astro-ph.GA].
- [13] R. Jansson and G. R. Farrar, *Astrophys. J. Lett.* **761**, L11 (2012), arXiv:1210.7820 [astro-ph.GA].

Upper limit on axion-photon coupling from Markarian 421

Supplemental Material

Hai-Jun Li, Wei Chao, and Yu-Feng Zhou

This is not the first investigation to constrain the axion-photon coupling from the TeV blazar Markarian 421. In Ref. [8], they first investigated the axion-photon conversion effect from this source by using the 4.5 years gamma-ray data of Fermi-LAT and Astrophysical Radiation with Ground-based Observatory at YangBaJing (ARGO-YBJ), showing the upper limit $g_{a\gamma} \lesssim 2 \times 10^{-11} \text{ GeV}^{-1}$ for the axion mass $[5.0 \times 10^{-10} \text{ eV} \lesssim m_a \lesssim 5.0 \times 10^{-7} \text{ eV}]$. In Ref. [9], they presented the axion limits from Markarian 421 by using the 1 year data of Fermi-LAT and Major Atmospheric Gamma Imaging Cherenkov Telescopes (MAGIC), showing the similar upper limits but for the axion mass $[8.0 \times 10^{-9} \text{ eV} \lesssim m_a \lesssim 2.0 \times 10^{-7} \text{ eV}]$. While in this work, we obtain a more stringent upper limit from the VHE gamma-ray data of Fermi-LAT and HAWC, which is even the most stringent limit compared with other astrophysical results in the axion mass $[1.0 \times 10^{-9} \text{ eV} \lesssim m_a \lesssim 1.0 \times 10^{-8} \text{ eV}]$. This is mainly because the large value of r_{VHE} obtained in this work. We know that here the greatest impact on the final result are parameters B_0 and r_{VHE} , both larger of them will lead to more stringent limit. We also discuss the impact of the parameter uncertainty of B_0 in the Supplemental Material. On the other hand, compared with the experimental data of ARGO-YBJ and MAGIC, the data of HAWC shows smaller uncertainty in the high energy region.

An interesting point in this work is the minimum best-fit chi-square χ_{min}^2 at $\{m_a \simeq 2.5 \times 10^{-9} \text{ eV}, g_{a\gamma} \simeq 2.5 \times 10^{-11} \text{ GeV}^{-1}\}$, we also note that the small chi-square χ_{axion}^2 in this region in other works [8], especially in Ref. [5] with the NGC 1275 observations set by Fermi-LAT. It is still unclear whether there are any new interpretations for this parameter region.

This Supplemental Material is organized as follows. In Sec. I, we show the gamma-ray SEDs of Markarian 421 under the null hypothesis. In Sec. II, we display the final photon survival probability. In Sec. III, we show the TS distribution. In Sec. IV, we discuss the impact of the parameter uncertainty. Then we make the axion analysis for the source Markarian 501 in Sec. V. Finally, we attach the experimental gamma-ray data of Markarian 421 and Markarian 501 in Sec. VI.

I. SEDS UNDER THE NULL HYPOTHESIS

In this section, we show the gamma-ray SEDs of Markarian 421 under the null hypothesis with the different intrinsic spectral models. It can be described by the simple and smooth concave functions with three to five free parameters. We take the common spectral models as the power law with exponential cut-off (EPWL, with three parameters), the power law with super-exponential cut-off (SEPWL, with four parameters), the log-parabola (LP, with four parameters), and the log-parabola with exponential cut-off (ELP, with five parameters),

$$\text{EPWL} : \Phi_{\text{int}}(E) = N_0 \left(\frac{E}{E_0} \right)^{-\Gamma} \exp \left(-\frac{E}{E_c} \right), \quad (\text{S1})$$

$$\text{SEPWL} : \Phi_{\text{int}}(E) = N_0 \left(\frac{E}{E_0} \right)^{-\Gamma} \exp \left(-\left(\frac{E}{E_c} \right)^d \right), \quad (\text{S2})$$

$$\text{LP} : \Phi_{\text{int}}(E) = N_0 \left(\frac{E}{E_0} \right)^{-\Gamma - b \log \left(\frac{E}{E_0} \right)}, \quad (\text{S3})$$

$$\text{ELP} : \Phi_{\text{int}}(E) = N_0 \left(\frac{E}{E_0} \right)^{-\Gamma - b \log \left(\frac{E}{E_0} \right)} \exp \left(-\frac{E}{E_c} \right), \quad (\text{S4})$$

where N_0 , Γ , E_0 , E_c , b , and d are free parameters. While for the models EPWL and SEPWL, we fix $E_0 = 1 \text{ GeV}$. Using these intrinsic spectral models, we fit the gamma-ray of Markarian 421 and list the corresponding best-fit chi-squares in Table I. Due to the smallest value of $\chi_{\text{null}}^2/\text{d.o.f.}$ for SEPWL, we finally select this spectral model to fit Markarian 421. The best-fit SEDs for other spectral models are also shown in Fig. S1.

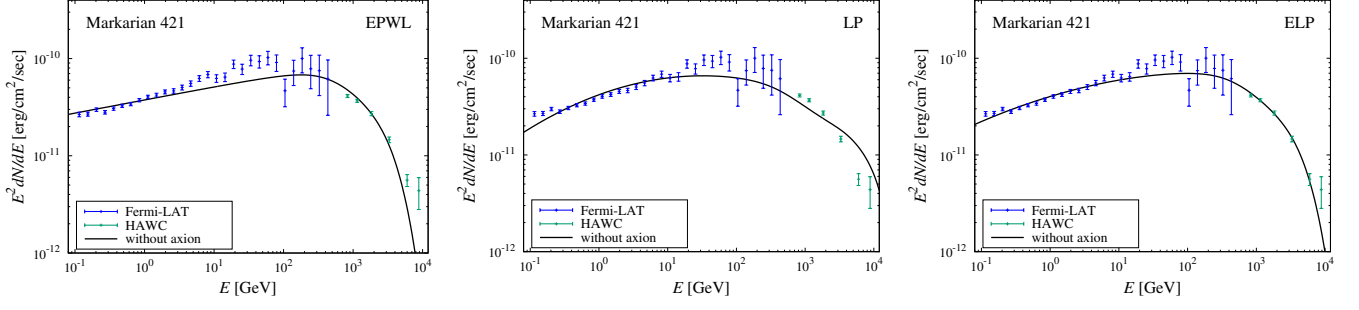


FIG. S1. The best-fit SEDs of Markarian 421 under the null hypothesis with the intrinsic spectral models EPWL (left), LP (middle), and ELP (right). The blue and green experimental data are taken from Fermi-LAT and HAWC, respectively.

TABLE I. The best-fit chi-square values under the null hypothesis of Markarian 421.

Model	parameter number	χ_{null}^2	$\chi_{\text{null}}^2/\text{d.o.f.}$
EPWL	3	158.97	4.82
SEPWL	4	44.24	1.38
LP	4	244.52	7.64
ELP	5	63.25	2.04

II. FINAL PHOTON SURVIVAL PROBABILITY

In the transverse homogeneous magnetic field B_T , the axion-photon conversion probability can be described by $\mathcal{P}_{a\gamma} = (g_{a\gamma} B_T L_{\text{osc}}/2\pi)^2 \sin^2(\pi x_3/L_{\text{osc}})$ with the oscillation length

$$L_{\text{osc}} = 2\pi \left[\left[\frac{|m_a^2 - \omega_{\text{pl}}^2|}{2E} + E \left(\frac{7\alpha}{90\pi} \left(\frac{B_T}{B_{\text{cr}}} \right)^2 + \rho_{\text{CMB}} \right) \right]^2 + g_{a\gamma}^2 B_T^2 \right]^{-1/2}, \quad (\text{S5})$$

where ω_{pl} is the plasma frequency, E is the axion/photon energy, α is the fine-structure constant, B_{cr} is the critical magnetic field, and ρ_{CMB} represents the cosmic microwave background (CMB) photon dispersion effect.

Here we show in Fig. S2 the final photon survival probability $\mathcal{P}_{\gamma\gamma}$ for Markarian 421. In the left and middle panels, we show $\mathcal{P}_{\gamma\gamma}$ for several typical axion-photon coupling $\{m_a, g_{a\gamma}\}$ parameter sets. In addition, we also show in the right panel the final photon survival probability for the minimum best-fit chi-square $\chi_{\text{min}}^2 = 31.47$ in the $\{m_a, g_{a\gamma}\}$ plane, with $\{m_a \simeq 2.5 \times 10^{-9} \text{ eV}, g_{a\gamma} \simeq 2.5 \times 10^{-11} \text{ GeV}^{-1}\}$.

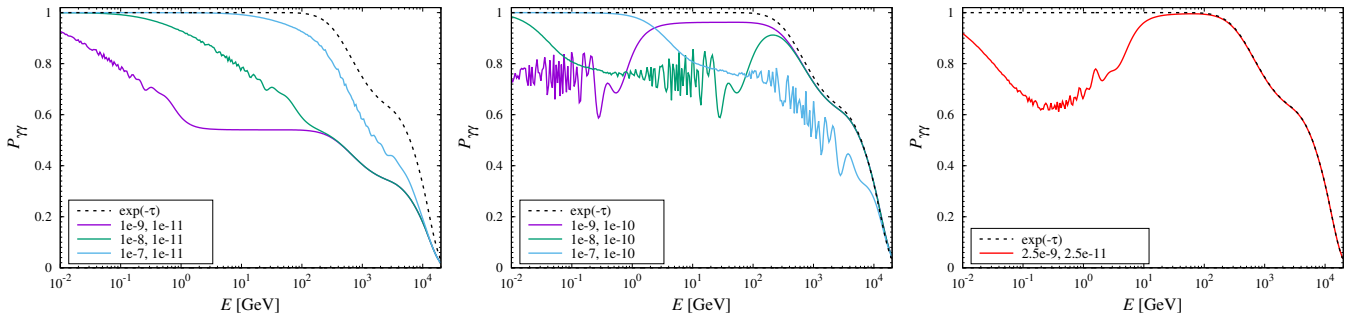


FIG. S2. The final photon survival probability for Markarian 421. The dashed line represents the pure EBL absorption effect with a factor $e^{-\tau}$. The solid lines correspond to the final photon survival probability with typical examples. The label $\{x, y\}$ represents the parameter set $\{m_a = x \text{ eV}, g_{a\gamma} = y \text{ GeV}^{-1}\}$. Note that the right panel corresponds to χ_{min}^2 .

III. TS DISTRIBUTION

We also show the test statistic (TS) distribution in Fig. S3 with the probability density function (PDF) and cumulative distribution function (CDF). In our simulations, we have the non-centrality $\lambda = 0.01$ and the effective d.o.f. = 5.29, indicating the 99% C.L. chi-square difference $\Delta\chi_{99\%}^2 \simeq 15.51$, and the threshold chi-square $\chi_{99\%}^2 = 31.47 + 15.51 = 46.98$. Then we use this value to set the 99% C.L. limit in the axion parameter plane.

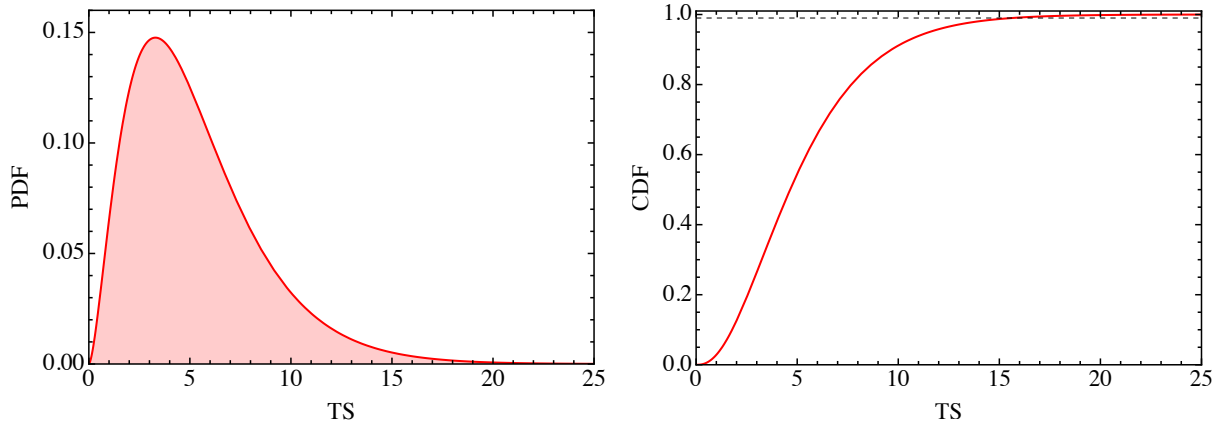


FIG. S3. The TS distribution with the PDF (left) and CDF (right). The dashed line corresponds to CDF = 0.99.

IV. IMPACT OF THE PARAMETER UNCERTAINTY

Since we take the Markarian 421 blazar jet core magnetic field at r_{VHE} as $B_0 = 24 \pm 6$ mG, here we discuss the impact of the uncertainty of B_0 . We show in Fig. S4 the best-fit chi-square χ_{axion}^2 distribution in the $\{m_a, g_{a\gamma}\}$ plane with different values of B_0 . Compared with $B_0 = 24$ mG, the 99% C.L. axion-photon limits are also shown in Fig. S5 with different lines. As we expected, the larger B_0 leads to the more stringent limit. The parameter r_{VHE} has a similar impact on the final result. In addition, since we take $\delta_{\text{D}} = 25 \pm 1$ and it has little impact on the limit, here we do not show the impact of the uncertainty of δ_{D} .

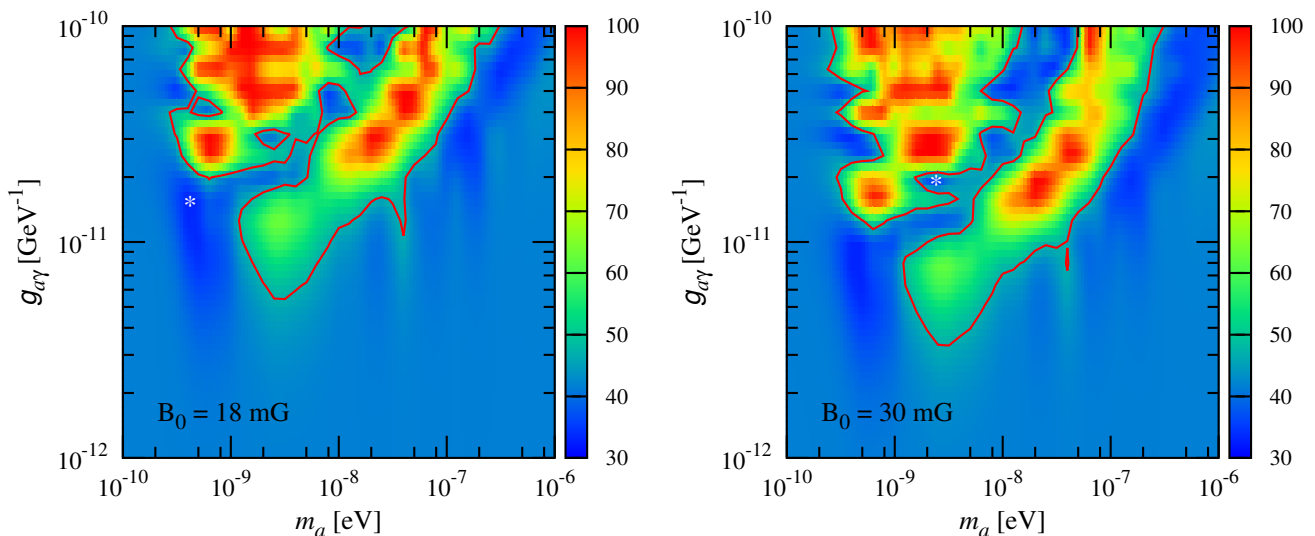


FIG. S4. The best-fit χ_{axion}^2 distribution in the $\{m_a, g_{a\gamma}\}$ plane for Markarian 421 with different B_0 . Left: we set $B_0 = 18$ mG, the label “*” corresponds to $\chi_{\text{min}}^2 = 32.94$ at $\{m_a \simeq 4.0 \times 10^{-10}$ eV, $g_{a\gamma} \simeq 1.6 \times 10^{-11}$ GeV $^{-1}$ }. Right: we set $B_0 = 30$ mG, the label “*” corresponds to $\chi_{\text{min}}^2 = 31.87$ at $\{m_a \simeq 2.5 \times 10^{-9}$ eV, $g_{a\gamma} \simeq 2.0 \times 10^{-11}$ GeV $^{-1}$ }. The red contour line represents the 99% C.L. limit.

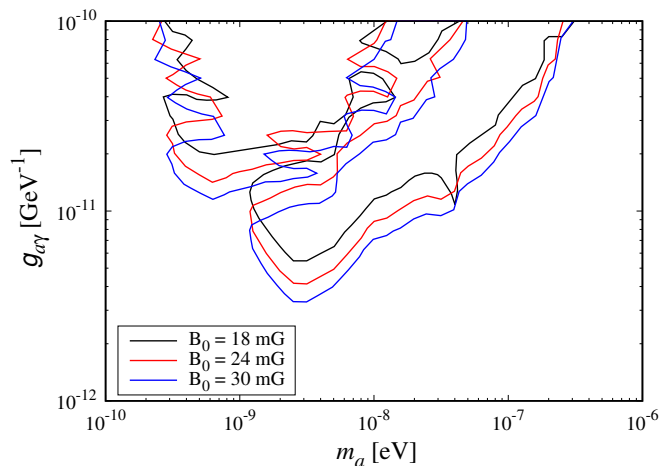


FIG. S5. The 99% C.L. axion-photon limits in the $\{m_a, g_{a\gamma}\}$ plane for Markarian 421 with $B_0 = 18$ mG, 24 mG, and 30 mG.

V. AXION ANALYSIS FOR MARKARIAN 501

Additionally, since the VHE gamma-ray observations of another TeV blazar Markarian 501 (Mrk 501, with redshift $z = 0.034$) at the same time are also measured by Fermi-LAT and HAWC, in the following we make the axion analysis for this source. The experimental data of Fermi-LAT (27 points) and HAWC (6 points) are shown in Fig. S6. Here we also select the gamma-ray intrinsic spectral model SEPWL to fit Markarian 501, and the best-fit SED corresponds to χ^2_{null} is shown in Fig. S6. The best-fit chi-squares for other spectral models are listed in Table II.

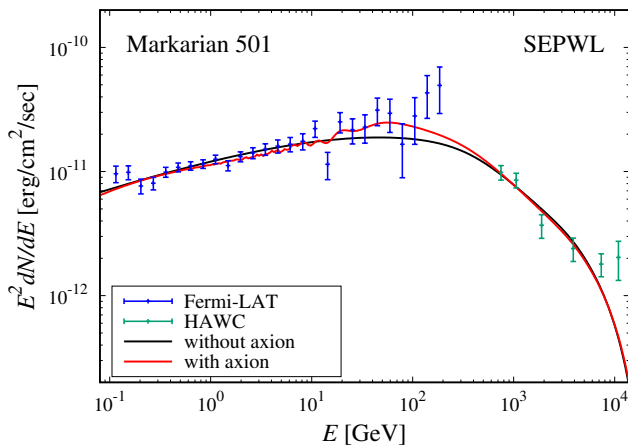


FIG. S6. The best-fit SEDs of Markarian 501 under the null and axion hypotheses. The black and red lines represent the best-fit SEDs without/with the axion-photon conversion, respectively. The blue and green experimental data are taken from Fermi-LAT and HAWC, respectively.

TABLE II. The best-fit chi-square values under the null hypothesis of Markarian 501.

Model	parameter number	χ^2_{null}	$\chi^2_{\text{null}}/\text{d.o.f.}$
EPWL	3	74.91	2.50
SEPWL	4	42.06	1.45
LP	4	53.61	1.85
ELP	5	50.68	1.81

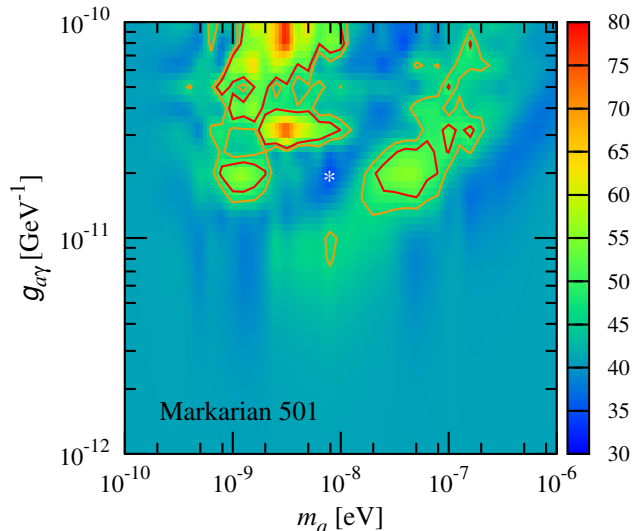


FIG. S7. The best-fit χ_{axion}^2 distribution in the $\{m_a, g_{a\gamma}\}$ plane for Markarian 501. The red and orange contours represent the 99% and 95% C.L. exclusion regions, respectively. The label “*” corresponds to $\chi_{\text{min}}^2 = 33.56$ at $\{m_a \simeq 7.9 \times 10^{-9} \text{ eV}, g_{a\gamma} \simeq 2.0 \times 10^{-11} \text{ GeV}^{-1}\}$.

For the blazar jet magnetic field of Markarian 501, we take $B_0 = 20 \pm 5 \text{ mG}$, $n_0 \simeq 1 \times 10^3 \text{ cm}^{-3}$, $R_{\text{VHE}} = 1.0 \times 10^{17} \text{ cm}$, $\theta_{\text{jet}} = 3.0^\circ$, $r_{\text{VHE}} \simeq 19.1 \times 10^{17} \text{ cm}$, and $\delta_{\text{D}} = 13 \pm 0.7$. Then we obtain the best-fit chi-square χ_{axion}^2 distribution in the $\{m_a, g_{a\gamma}\}$ plane, which is shown in Fig. S7. The value of the minimum best-fit chi-square in the $\{m_a, g_{a\gamma}\}$ plane is $\chi_{\text{min}}^2 = 33.56$ at $\{m_a \simeq 7.9 \times 10^{-9} \text{ eV}, g_{a\gamma} \simeq 2.0 \times 10^{-11} \text{ GeV}^{-1}\}$, see also the corresponding SED in Fig. S6. In our TS analysis, we have the non-centrality $\lambda = 0.01$ and the effective d.o.f. = 6.11, indicating the 99% C.L. threshold chi-square $\chi_{99\%}^2 = 50.60$, corresponding to the red contour in Fig. S7. Since it shows a weak limit, we also show the 95% C.L. limit ($\chi_{95\%}^2 = 46.38$) with the orange contour. While for Markarian 421, since the value of $\chi_{95\%}^2$ is smaller than the best-fit chi-square under the null hypothesis χ_{null}^2 , we just show the 99% C.L. limit. In summary, here we do not obtain a stringent upper limit from the source Markarian 501.

VI. EXPERIMENTAL GAMMA-RAY DATA

Finally, we attach the experimental gamma-ray data of Markarian 421 and Markarian 501 measured by Fermi-LAT and HAWC in Table III and IV, respectively.

TABLE III. The experimental gamma-ray data of Markarian 421. The third and fourth columns are the flux and its uncertainty.

Collaboration	E (GeV)	$E^2 dN/dE$ (erg/cm ² /sec)	δ (erg/cm ² /sec)
Fermi-LAT	0.1152	2.662e-11	1.457e-12
Fermi-LAT	0.1531	2.686e-11	1.297e-12
Fermi-LAT	0.2034	2.984e-11	1.220e-12
Fermi-LAT	0.2701	2.805e-11	1.186e-12
Fermi-LAT	0.3588	3.059e-11	1.204e-12
Fermi-LAT	0.4766	3.268e-11	1.247e-12
Fermi-LAT	0.633	3.405e-11	1.324e-12
Fermi-LAT	0.8409	3.733e-11	1.472e-12
Fermi-LAT	1.117	4.030e-11	1.667e-12
Fermi-LAT	1.484	4.214e-11	1.852e-12
Fermi-LAT	1.971	4.542e-11	2.143e-12
Fermi-LAT	2.618	4.647e-11	2.466e-12
Fermi-LAT	3.477	5.040e-11	2.922e-12
Fermi-LAT	4.619	5.540e-11	3.508e-12
Fermi-LAT	6.135	6.246e-11	4.246e-12
Fermi-LAT	8.15	6.849e-11	5.077e-12
Fermi-LAT	10.82	6.250e-11	5.583e-12
Fermi-LAT	14.38	6.444e-11	6.508e-12
Fermi-LAT	19.1	8.767e-11	8.731e-12
Fermi-LAT	25.37	7.798e-11	9.440e-12
Fermi-LAT	33.7	9.612e-11	1.198e-11
Fermi-LAT	44.76	9.335e-11	1.353e-11
Fermi-LAT	59.46	1.023e-10	1.630e-11
Fermi-LAT	78.98	9.133e-11	1.762e-11
Fermi-LAT	104.9	4.667e-11	1.477e-11
Fermi-LAT	139.4	7.443e-11	2.167e-11
Fermi-LAT	185.1	1.001e-10	2.888e-11
Fermi-LAT	245.9	7.840e-11	2.949e-11
Fermi-LAT	326.6	7.500e-11	3.342e-11
Fermi-LAT	433.8	6.148e-11	3.538e-11
HAWC	831.3	4.124e-11	1.474e-12
HAWC	1145	3.678e-11	1.371e-12
HAWC	1835	2.713e-11	1.323e-12
HAWC	3306	1.463e-11	9.799e-13
HAWC	5984	5.615e-12	7.881e-13
HAWC	8809	4.379e-12	1.578e-12

TABLE IV. Same as Table III but for Markarian 501.

Collaboration	E (GeV)	$E^2 dN/dE$ (erg/cm ² /sec)	δ (erg/cm ² /sec)
Fermi-LAT	0.1153	9.598e-12	1.459e-12
Fermi-LAT	0.1531	9.851e-12	1.259e-12
Fermi-LAT	0.2034	7.649e-12	1.041e-12
Fermi-LAT	0.2701	8.056e-12	9.441e-13
Fermi-LAT	0.3588	9.912e-12	9.147e-13
Fermi-LAT	0.4764	1.083e-11	8.899e-13
Fermi-LAT	0.6332	1.112e-11	8.724e-13
Fermi-LAT	0.8408	1.152e-11	9.082e-13
Fermi-LAT	1.117	1.256e-11	9.967e-13
Fermi-LAT	1.484	1.117e-11	1.039e-12
Fermi-LAT	1.971	1.319e-11	1.219e-12
Fermi-LAT	2.618	1.413e-11	1.436e-12
Fermi-LAT	3.477	1.513e-11	1.609e-12
Fermi-LAT	4.62	1.604e-11	1.935e-12
Fermi-LAT	6.137	1.662e-11	2.205e-12
Fermi-LAT	8.152	1.755e-11	2.624e-12
Fermi-LAT	10.82	2.217e-11	3.312e-12
Fermi-LAT	14.38	1.144e-11	2.829e-12
Fermi-LAT	19.1	2.516e-11	4.681e-12
Fermi-LAT	25.37	2.165e-11	4.962e-12
Fermi-LAT	33.7	2.281e-11	5.872e-12
Fermi-LAT	44.75	3.127e-11	7.846e-12
Fermi-LAT	59.47	2.949e-11	8.848e-12
Fermi-LAT	78.99	1.660e-11	7.688e-12
Fermi-LAT	104.9	2.801e-11	1.143e-11
Fermi-LAT	139.4	4.310e-11	1.626e-11
Fermi-LAT	185.1	4.946e-11	2.010e-11
HAWC	749.8	9.850e-12	1.318e-12
HAWC	1060	8.533e-12	1.155e-12
HAWC	1890	3.696e-12	8.000e-13
HAWC	3890	2.397e-12	5.134e-13
HAWC	7362	1.797e-12	3.769e-13
HAWC	10900	2.035e-12	7.075e-13